TiO₂/WO₃/Au nanoarchitectures' photocatalytic activity "from degradation intermediates to catalysts' structural peculiarities" Part II: Aerogel based composites – fine details by spectroscopic means

L. Baia [a,b], A. Vulpoi [a,b], T. Radu [a,b], É. Karácsonyi [c], A. Dombi [c], K. Hernádi [c], V. Danciu [d], S. Simon [a,b], K. Norén [e], S.E. Canton [f], G. Kovács [a,d,**], Zs. Pap [a,c,d,*]

[a] Faculty of Physics, Babeş-Bolyai University, M. Kogălniceanu 1, RO-400084 Cluj-Napoca, Romania
[b] Institute for Interdisciplinary Research on Bio-Nano-Sciences, Treboniu Laurian 42, RO-400271 Cluj-Napoca, Romania
[c] Research Group of Environmental Chemistry, Institute of Chemistry, University of Szeged, Tisza Lajos krt. 103, HU-6720 Szeged, Hungary
[d] Faculty of Chemistry and Chemical Engineering, Babeş-Bolyai University, Arany János 11, RO-400028 Cluj-Napoca, Romania
[e] Chemical Physics Department, Chemical Centre, Lund University, Getingevägen 60, S-22241 Lund, Sweden
[f] Department of Synchrotron Radiation Instrumentation, Lund University, P.O. Box 118, S-22100 Lund, Sweden

ARTICLE INFO

ABSTRACT

The "build-up" methodology of a composite photocatalyst is a critical issue regarding the showed photocatalytic performance, including the formation of intermediates. To investigate this issue TiO₂/WO₃/Au aerogel composites were obtained by sol–gel method and subsequent photoreduction (Au) with UV or visible light. The obtained composites' photocatalytic activity and intermediate formation profiles were evaluated using phenol as a model pollutant. XPS/UPS, XAFS and DRS were used to uncover local coordination, surface chemistry (of the different types of atoms (Ti, W, O and Au) and the band-structure (band-gap, possible electron transitions) of the obtained nanomaterials. The intermediates' evolution profile and structural peculiarities were successfully correlated and it was shown that each minor structural (bulk or surface) change has a significant impact on the photocatalytic activity and intermediate formation dynamics.

© 2013 Elsevier B.V. All rights reserved.

1. Introduction

Photocatalysts are using energy from light to generate oxidative reactants, building reliable pathways to air disinfection, decontamination of water and hydrogen generation. The most important aspects of the perfect photocatalyst are the accessibility of the material (to be relative inexpensive), the high oxidativity of the photogenerated holes and the high stability of the material [1]. One of the semiconductors that fulfill very well the above mentioned characteristics is TiO₂. The "story" of this photocatalyst began in late 1960's with solar energy conversion [2] and developed into commercially available self-cleaning products, antifogging surfaces and environmentally applicable decontaminators.

On the other hand, behind the advantages and promises shown by TiO₂ a few draw-backs and weaknesses can be found. Its most representative weakness is the relatively large band-gap ($E_g \geq 3$–3.2 eV) that enables just the absorption of less than 4–10% of the solar radiation. In order to extend the absorbable light region to the visible spectrum and to increase the yield of absorption, coupling with other oxides (e.g. SnO₂ [3,4], SiO₂ [5,6] and WO₃ [7,8]) have gained high attention among the scientific community. Coupling TiO₂ with WO₃ semiconductor, used as photocatalyst can increase the efficiency of the photocatalytic process by improving the charge separation, extending the energy range of the photoexcitation, offering a relatively small band-gap ($E_g \approx 2.4$–2.8 eV) and a long-term stability [9,10]. Using the relatively smaller band-gap of WO₃ comparing to TiO₂ the electrons can be transferred from titania to WO₃ and further, minimizing thus the recombination losses of the photoexcitation process [11].

Beside the already described improvement of the photocatalytic activity in the previous part of this article, obtained by the deposition of noble-metal nanoparticles on the semiconductor surface [12], another method to obtain TiO_2-based photocatalysts is the sol–gel method followed by supercritical drying [13–15]. By the means of this procedure the solvent is removed, while the surface tension effect and coagulation of nanoparticles are drastically attenuated, obtaining finally nanomaterials with high porosity and specific surface area that can be useful in achieving higher efficiencies in the photocatalytic processes. Additionally, it should be taken in consideration the fact that after thermal treatment these aerogels like samples are quiet efficient photocatalysts (despite their drastic surface area decrease). Furthermore, a very important aspect can be that during the formation of aerogels with two or more oxide components the appearance of mixed oxides is most likely. Additionally, doping phenomena can more easily occur (due to the gelification process's nature), resulting visible light active photocatalysts [16].

Even if all the above presented methods used for the enhancement of photocatalytic characteristics of TiO_2 have shown promising results, to our best knowledge the merging of the approaches described above was not investigated, namely having two different types of nanomaterials (a noble metal – Au; and another semiconductor oxide – WO_3) which are capable to inhibit significantly the recombination process of the generated charge carriers [7].

Furthermore, the number of studies regarding the photodegradation intermediates' evolution profile is sparse. This aspect is critical, because it can occur that one of the resulting by-products of the degradation is more toxic than the starting compound, as in the case of phenol.

Phenol and phenolic compounds are widely used in many industries, being one of the organic materials which are often found in wastewater. Among other wastewater treatment methods, heterogeneous photocatalysis can be used to eliminate these kinds of organic compounds [17]. On the other side, during the photodegradation process of phenol, the appearance, in different proportions, of the hydroxylated phenol compounds such as hydrochinon, pyrocatechol and resorcinol was observed [18]. Some of these phenol intermediates are in the category 1 or 2 carcinogenetic risk and aquatic toxicity (according to Regulation (EC) No 1272/2008 [EU-GHS/CLP]). Having different toxicity levels, is crucial to adjust the structure of the photocatalyst in such a way, that the least toxic intermediate formation to be favored.

Consequently, the main aim of this work was to investigate by different spectroscopic methods (DRS, Raman spectroscopy, XAFS, etc.) the impact of sol–gel preparation method and the photodeposition of Au nanoparticles under UV/Vis light, on the crystallization of TiO_2/WO_3–Au ternary composites. Furthermore, crucial information links were provided to explain the photocatalytic activity of the obtained samples and to correlate the structural particularities with the intermediates evolution trends observed during the photodegradation process.

2. Experimental

2.1. Synthesis of the composites

The TiO_2–WO_3 samples were prepared by sol–gel method using titanium isopropoxide (TIPT, 98%; Merck), tungsten isopropoxide (TEOW), ethanol (C_2H_5–OH (EtOH)), H_2O, and nitric acid (HNO_3) applying the following molar ratios of TIPT/TEOW/EtOH/H_2O/HNO_3:

- 8.50/0.120/28/2.18/0.168 – for samples containing 4 wt.% WO_3.
- 8.50/0.921/28/2.18/0.168 – for samples containing 24 wt.% WO_3.

The gels were allowed to age for 14 days and then they were washed 3–4 times in different mixtures of alcohol/water ratios. In order to eliminate the excess water from the pores the samples were finally washed in pure EtOH. The gels were then supercritically dried with liquid CO_2 ($T > 35\,°C$, $p > 1200$ psi) by using a SAMDRI-PVT 3D (Tousimis) equipment. The as prepared aerogels were subjected to a thermal treatment at 700 °C for 2 h. Pure TiO_2 aerogel was also obtained by this method.

The gold deposition was performed under UV light (6×6 W Black Light Lamps, with $\lambda_{max} \approx 365$ nm) using 12 mM $HAuCl_4$ solution as gold precursor and 50 mM oxalic acid as hole scavenger, in a thermostated 200 mL Pyrex (filled with 175 mL suspension) reactor. The TiO_2/WO_3 catalyst concentration was 1 g/L, while the gold precursor quantity was calculated to have an equivalent of 1 wt.% Au on the suspended composite. The reduction process was performed for 4 h. The visible light deposition followed the procedure detailed previously, the only difference was that 6×6 W Philips fluorescent lamps (visible light emitting coating) were used and 1 M $NaNO_2$ was circulated in the thermostating jacket to eliminate any UV radiations. All the composites were washed several times in deionized water and dried at 80 °C for 24 h. The gold content was proven to be ≈ 1 wt.% in all the composite materials and no traces of the precursor was detected using UV–Vis spectrophotometry. Finally, the obtained TiO_2–WO_3/Au nanocomposites were coded as follows: Aero/WO_3(x)–Au–UV or VIS, where x represents the WO_3's concentration in the composite in wt.%, while UV or VIS marked the light used during the photodeposition process.

2.2. Methods and instrumentation

2.2.1. Characterization methods

X-ray diffraction (XRD) measurements were performed on a *Shimadzu 6000* diffractometer using Cu-Kα radiation ($\lambda = 1.5406$ Å), equipped with a graphite monochromator. The anatase–rutile phase ratio in TiO_2 was evaluated using the method used by Banfield [19], and the crystallites average size was calculated using the Scherrer equation [20].

The *FT-Raman* spectra were recorded by using a *Bruker Equinox 55* spectrometer with an integrated *FRA 106 Raman* module using a Nd-YAG laser (1064 nm). Raman measurements were recorded with a spectral resolution of 1 cm^{-1}.

JASCO-V650 spectrophotometer with an integration sphere (*ILV-724*) was used for measuring the *DRS spectra* of the samples ($\lambda = 300$–800 nm). The possible electron transitions were evaluated by plotting the dR/dλ vs. λ, where R is the reflectance and λ is the wavelength [21].

FEI Quanta 3D FEG dual beam – in high vacuum mode using EDT (Everhart Thornley Detector) electron microscope (equipped with an ApolloX SDD Energy Dispersive X-ray (EDX) detector) was used to obtain quantitative elemental analyses (i.e. gold content, which was found to be 1 ± 0.1 wt.% in each case). TEM images were obtained with a FEI Tecnai F20 field emission, high resolution Transmission Electron Microscope (TEM) operating at an accelerating voltage of 200 kV and equipped with Eagle 4k CCD camera (Fig. 1)

XPS measurements were performed on a SPECS PHOIBOS 150 MCD instrument, with monochromatized Al Kα radiation (1486.69 eV) at 14 kV and 20 mA, and a pressure lower than 10^{-9} mbar. Samples were mounted on the sample holder using double-sided adhesive carbon tape. High-resolution Au4f, Ti2p, and W4f spectra were recorded in steps of 0.05 eV for analyzed samples. Analysis of the obtained data was carried out with Casa XPS software. All peaks have been deconvoluted using Shirley background and Lorentzian–Gaussian line shapes. The applied value of the Gaussian–Lorentzian ratio was 30.

Microprocessor controlled surface area analyzer, Qsurf Series M1, was used for the *N_2 adsorption measurements*. Outgassing at
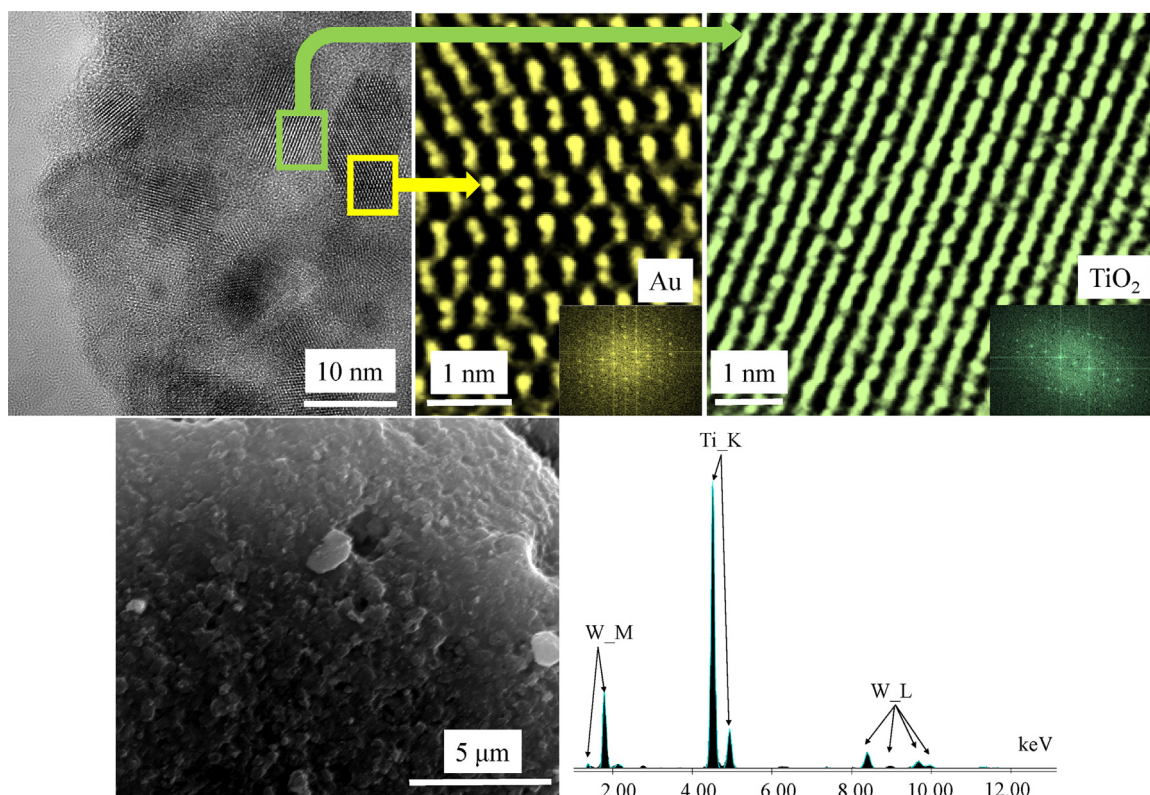
Fig. 1. SEM/HRTEM micrographs and EDX spectrum of sample Aero/WO$_3$(24%)–Au–UV (Au was detected around 1 wt.% and it is superposed partially in the EDX spectra by the W lines).

200 °C was performed for 30 min, to ensure maximum accuracy of the obtained information. The specific surface area of the samples was evaluated on the basis of Brunauer, Emmet and Teller (BET) equation.

The Ti K edge (4966 eV) and the W L3 edge (10206 eV) XAS spectra of the Aero/WO$_3$(24%), Aero/WO$_3$(24%)–Au–VIS and Aero/WO$_3$(24%)–Au–UV samples were measured on beam line I811 at the MAX-lab facility, Lund, Sweden [22]. This superconducting multipole wiggler beam line is equipped with a water-cooled channel cut Si (1 1 1) monochromator delivering at 10 keV, approximately 2×1015 photons/s/0.1% bandwidth with horizontal and vertical FWHM of 7 and 0.3 mrad, respectively. A beam size of 0.5 mm × 1.0 mm (width × height) was used. The incident beam intensity I0 was measured with an ionization chamber filled with a mixture of He/N$_2$. The data were acquired in fluorescence mode. The cell to detector distance was varied with concentration in order to avoid detector saturation. The spectra were analyzed in the EXAFS region with the VIPER software [23].

2.2.2. The assessment of the photocatalytic efficiencies

A photoreactor system with three LighTech 40 W fluorescent lamps ($\lambda_{\max} \approx 365$ nm, irradiation distance = 5 cm, irradiation time = 3 h) was used to measure *the photocatalytic activities*. The photocatalyst suspension containing phenol (initial concentration of phenol $c_{0, \text{phenol}} = 0.5$ mM; catalyst concentration $c_{\text{photocatalyst}} = 1.0$ g/L; total volume of the suspension $V_{\text{susp}} = 50$ mL) was continuously purged by air in order to maintain the dissolved oxygen concentration constant during the whole experiment. The concentration decrease of the chosen organic substrate (phenol) and their degradation intermediates were followed using an *Agilent 1100 series HPLC* system (Fig. S1 from the supplementary information, available online). The assessed error of the photocatalytic tests (based on reproducibility experiments) was 5–9%.

To quantify efficiently the intermediates' evolution the *intermediate evolution index* (IEI) was introduced, which was calculated, using the following formula, where F_{int} is the empirical intermediate concentration evolution function, C_{phendef} is the quantity of phenol degraded in the case of the less performing catalyst (0.105 mM phenol consumption in the present case), therefore a low IEI value means that the degradation intermediate does not accumulate in the reaction system [24].

$$\text{IEI} = \int_0^{C_{\text{phendef}}} F_{\text{int}} dC$$

The obtained reaction rates were normalized to the surface area of the photocatalysts to emphasize the surface quality's critical importance. These normalized data are in strong relationship with the surface structural data, which will be provided for each of the materials obtained. The normalization took place according to reference [24]:

$$r_{\text{normalised}} \left(\frac{\text{mM} \cdot \text{g}}{\text{m}^2 \cdot \text{h}} \right) = \frac{r(\text{mM} \cdot \text{min}^{-1})}{S_{\text{BET}}(\text{m}^2 \cdot \text{g}^{-1})} \cdot 60$$

3. Results and discussions

3.1. The photocatalytic activity of the obtained nanocomposites

3.1.1. Phenol degradation (Fig. 2a and b)

In the first part of the present work [24] it was shown that the highest activity was achieved by the P25 based composites containing gold, which was deposited under UV irradiation (P25/WO$_3$(x)–Au–UV), while the lowest performance was exhibited by the P25/WO$_3$(x)–Au–VIS composite (the gold was deposited under visible light irradiation). The activity trend persists also in the present case (Fig. 2a), the Aero/WO$_3$(x)–Au–VIS composites having
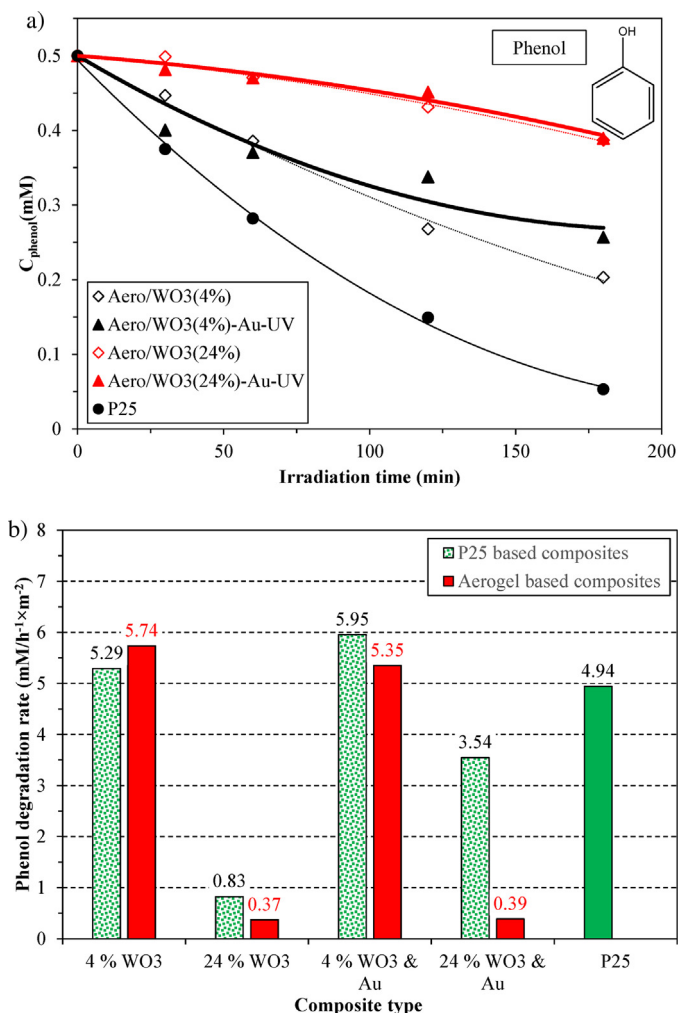
Fig. 2. (a) Phenol UV photodegradation curves of the prepared nanocomposites. (b) Normalized phenol degradation rates of the aerogel based nanocomposites compared with the appropriate P25 based materials and pure P25.

Fig. 3. The *simplified* mechanism (only the investigated intermediates are listed) of the formation of hydroxylated by-products during the photocatalytic runs. It should be noted here that the resorcinol formation is not favored, which is reflected by the low IEI numbers.

nearly no photocatalytic activity. *This lack of activity towards phenol was also observed for the WO$_3$ free aerogel likewise. Consequently, in the discussion of the activities and intermediate formation the mentioned samples will not be included. Furthermore, these materials will be "called upon" in the structural related discussions, if needed.*

In the first instance we have observed, that best performing composite was the Aero/WO$_3$(4%) with a phenol degradation rate of 2.17 μM/min, which was lowered by the presence of Au (1.88 μM/min–sample Aero/WO$_3$(4%)–Au–UV). The reaction rate decreased even more, to 0.35 μM/min (Aero/WO$_3$(24%)), with the increase of the WO$_3$ content (24 wt.%). These differences were even higher, if it was taken into account the specific surface area and it was normalized the degradation rate to it[1]. Applying this "correction" it can be seen that the differences are much larger in the degradation rates (5.74 mM/h × m^2 for Aero/WO$_3$(4%), while this value decreases to ≈0.37 mM/h × m^2 in Aero/WO$_3$(24%)). If the normalized values are considered, it can be clearly observed that our materials are 1.15 times more efficient, than Aeroxide P25.

Furthermore, as can be seen in Fig. 2b, in all cases (both P25 and Aerogel based samples) [24] the addition of tungsten oxide was
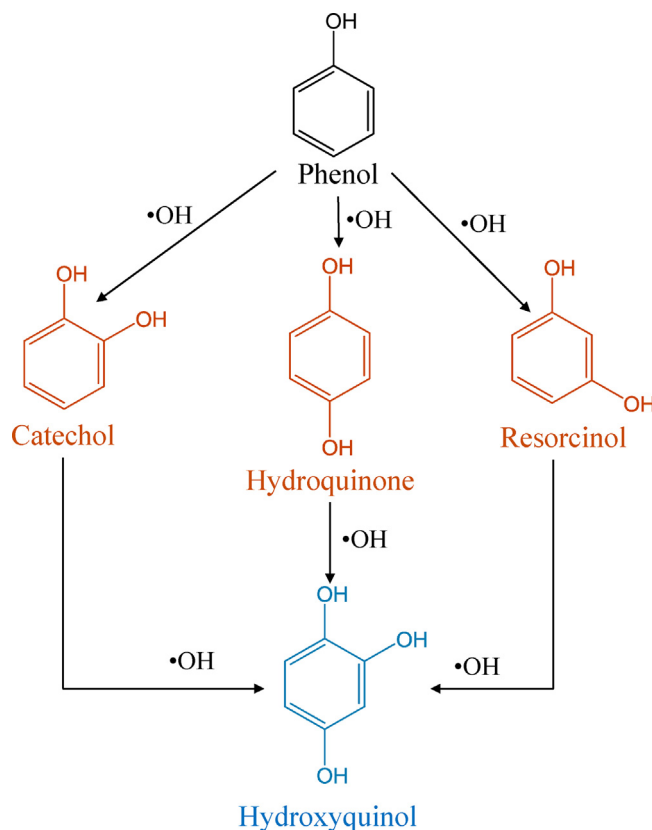
quite beneficial, excepting the case of 24 wt.% WO$_3$. The addition of gold, increased the degradation rate only for the P25 based composites [24] (for sample P25/WO$_3$(24%) a 4 fold increase was registered in the activity after gold deposition from 0.83 to 3.54 mM/h × m^2), while in the case of the aerogel based samples, the noble metal deposition seemed to be ineffective in terms of degradation rate. The probable reason of the enhancement observed in the case of the P25 based composites may be caused by the fact that the gold usually is deposited on the surface of the rutile crystalline phase [25], which is advantageous in the charge carrier migration process: the electron migrates further from the rutile to the gold nanoparticle, further enhancing the charge separation. Unfortunately, this enhancement provided by the presence of the rutile is not "available" in the presently investigated aerogel systems.

If we intend to study not just the simply the efficiency but also the applicability of different samples described above, we have to take into consideration the appearance of intermediates as well, which can raise toxicity problems, already described in the first part of this work.

3.1.2. Phenol degradation intermediates – Table 1

All photocatalytic materials, during their "activity" yield a defined number of intermediates (Fig. 3). We focused in the previous part of this work on four hydroxylated by-products: hydroquinone (HC), pyrocatechol (PY), resorcinol (RES) and 1,2,4-trihydroxy-benzene (124THB). To emphasize the effect of the different synthetic route (sol–gel, trough aerogel) on the intermediate formation of the studied composites, the present work compares the evolution trend of these compounds for both cases (P25 based [24] and TiO$_2$ aerogel based materials) (Table 1).

---

[1] Please note that in the case of the normalized reaction rate the μM term was substituted with mM, to yield more easily interpretable values for the readers.
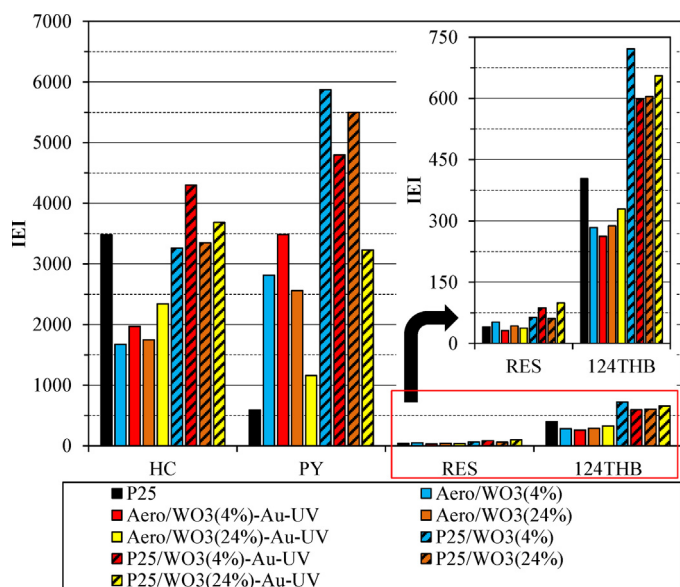
Fig. 4. Phenol UV photodegradation intermediates' IEI values compared among the different composites.

Fig. 4 shows clearly that, the aerogel materials yield 50% less intermediates during the degradation process, while their activity is comparable with the composites based on P25 [24] (this means that that the aerogel based materials are not so efficient in producing OH radicals, instead they are probably oxidizing the complexated phenol attached to the WO_3 entities as we proved in the first part of this work by NMR spectroscopy [24]). This is a quite important result, which points out the importance of choosing the appropriate synthesis route for designing the desired sample. To discover more details related to the IEI values obtained, each studied intermediate evolution trend should be taken under the loupe.

The tungsten oxide content in the composite systems does not have a major influence on the HC IEI values. However, after UV induced gold deposition on these materials, the IEI value rises. The situation is quite different in the case of PY. The presence of WO_3 increases considerably the IEI values of the aerogel type materials. After gold deposition, the IEI obtained for Aero/WO_3(24%)–Au–UV is significantly lower, while higher values were noticed if the gold was deposited on the Aero/WO_3(4%) samples (resulting the composite Aero/WO_3(4%)–Au–UV). Interestingly, in the case of P25 based samples [24], such as P25/WO_3(4%)–Au–UV and P25/WO_3(24%)–Au–UV an increase was observed in the intermediate evolution index.

The IEI values for the RES and 124THB are much smaller compared to the HC and PY. It seems that the trend remains the same as

discussed previously, namely, the presence of WO_3 enhances the production of hydroxylated products. The WO_3 content does not influence decisively the IEI among the aerogel based composites for RES and 124THB. The UV gold deposition seems to be important in the case of Aero/WO_3(24%)–Au–UV, while a slightly higher quantity of 124THB is produced. Additionally, it should be mentioned here, that compared to the bare P25, the TiO_2 aerogel based materials results in a smaller IEI number. The only exception regarding this aspect was the IEI for PY.

3.2. Structural/optical aspects of the TiO_2/WO_3/Au composites

3.2.1. X-ray diffraction (XRD) – Crystal phase composition and particle size – Fig. 5

The first step in the evaluation process of the structural features of these materials was to obtain critical information regarding the crystal phase composition and particle size. The pure titania aerogel system was composed from ≈10 wt.% rutile and 90 wt.% anatase. As tungsten oxide is added to the composite system the anatase phase remained stable at 700 °C (usually, this transformation takes place around 400–500 °C [26]), meaning that the WO_3's presence stabilizes the anatase phase (similarly to SiO_2/TiO_2 composites [27]). Interestingly, at 4 wt.% of WO_3 no crystalline WO_3 is observable (similar phenomena was observed when studying the P25 based composites [24], when W doping and amorphous WO_3 were detected). In the case of the 24 wt.% WO_3 containing materials two weak diffraction peaks (monoclinic WO_3) appears at $2\theta° = 24$ and 34. This means that the WO_3 crystallizes if is present in higher "concentration" (i.e. 24 wt.%). The gold deposition under UV or visible light does not affect the crystal phase composition (Fig. 5).

The crystallites' size of TiO_2 was not influenced by the gold reduction on the samples' surface. Consequently, in the case of the nanomaterials containing 4 wt.% WO_3, the estimated mean particle size was of 20 and 11 nm for the nanocomposites with 24% WO_3, respectively (Fig. 1). Furthermore, it should be noted here that with the increase of the WO_3 content in the samples, the size of the TiO_2 crystallites decreases. This aspect represents a major difference compared to the P25 based samples and has major consequences in the activity–intermediates–structure relation.

Although, critical information was gained regarding the crystallites' size and phase composition of the samples there are open questions related to the nature of the WO_3 in these materials. To clarify these uncertain aspects, their DRS spectra were further analyzed.

3.2.2. Diffuse reflectance spectroscopy (DRS)–optical properties – Fig. 6

After supercritical drying and thermal treatment the titania based aerogels are white powders, meaning that this material absorbs mostly UV light, similar to the commercial P25. Analyzing

Table 1
Phenol UV photodegradation rates, significant structural parameters and IEI values of the obtained nanocomposites.

| Sample name	Phenol degradation rate (μM/min)	S_{BET} (m²/g)	Normalized phenol degradation rates (mM/h × m⁻²)	Crystallites mean size (nm)		Intermediate evolution index (IEI)			
				TiO_2 Anatase/Rutile	WO_3 Monoclinic	HC	PY	RES	124THB
Aero/WO_3(4%)	2.17	22.7	5.73	19/–	–	1672	2814	52.15	283.7
Aero/WO_3(4%)–Au–VIS	–	25.4	–	20/–	–	–	–	–	–
Aero/WO_3(4%)–Au–UV	1.88	21.1	5.34	20/–	–	1972	3488	31.27	262.4
P25	4.12	50.0	4.94	25/40	–	3480	595.1	40.07	403.2
Aero/WO_3(24%)	0.35	56.6	0.37	11/–	n.q.	1751	2558	42.76	287.6
Aero/WO_3(24%)–Au–VIS	–	48.2	–	11/–	n.q.	–	–	–	–
Aero/WO_3(24%)–Au–UV	0.30	46.6	0.38	11/–	n.q.	1672	2814	52.15	283.7

n.q., not quantifiable.
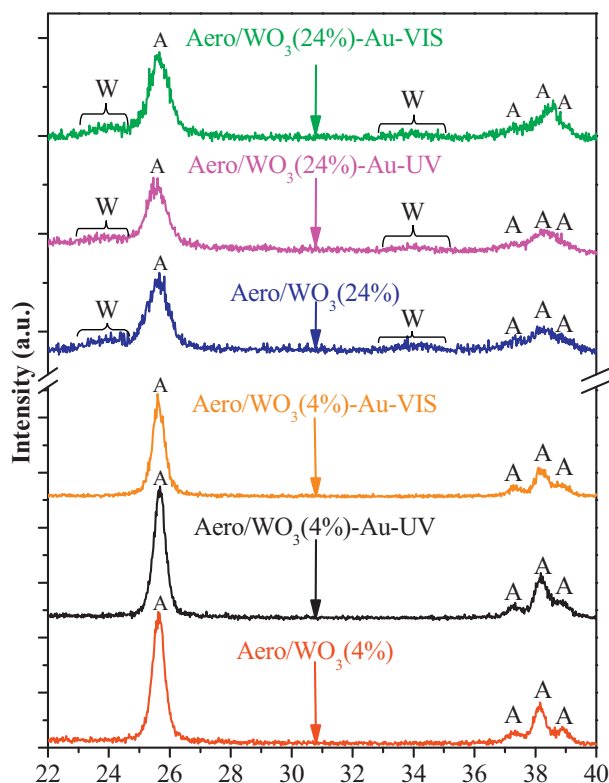
Fig. 5. XRD patterns of all the studied nanocomposites (W = monoclinic WO$_3$, A = anatase TiO$_2$).

the first derivate of the DRS spectra of these composites we can observe one possible electron transitions, which is responsible for the absorption of UV light, corresponding to the band-gap value of anatase ($\approx$370 nm). Furthermore, another peak is observable at $\approx$397 nm, which could be assigned to the rutile phase of the TiO$_2$ component, but that is not present in these materials. So, probably this new peak can be attributed to the doping process of these materials (transitions occurring within the band-gap [28]). Additionally, another component of the first derivative is observable near $\approx$453 nm, which corresponds to the formation of individual WO$_3$ nanoparticles, as demonstrated in the first part of this work series [24] (Fig. 6).

The most enthralling fact was the difference shown within the ratio of the above mentioned peaks, which could yield essential information about defect structures' quantum size effect [21] (originating from the microstructure of the material) and their con-

tribution to the band-gap structure and band shifts [21]. In our specific case it can be seen that after the increase of the tungsten oxide content to 24 wt.%, the ratio between the peak at 397 and that at 370 nm increases significantly, while a new peak at 453 nm appears. This clearly suggests that the doped titania phase is dominant, along with the crystallized WO$_3$ particles.

Following the gold deposition process one can see that in the case of Aero/WO$_3$(4%)–Au–UV composite only the "anatase" peak remains, suggesting a major change in the "nature" of the WO$_3$ in this material. The situation gets even more interesting when Au was deposited on the Aero/WO$_3$(24%) composite's surface. While the transition located at 453 nm remains intact, the peak at 397 nm diminishes considerably in Aero/WO$_3$(24%)–Au–UV, which was observed in the case of the materials with 4 wt.% WO$_3$.

Thus, the optical properties of these nanocomposites suggests that the WO$_3$ can be found both as crystalline WO$_3$ (supported by both XRD, DRS) and as doping W (by DRS). However, based on the XRD patterns we can strongly suppose the presence of amorphous WO$_3$.

Additionally, the DRS spectra revealed the asymmetry of the plasmonic band towards higher wavelengths that denotes the increase of the aggregated Au nanoparticle's number [29,30], as in the case of P25 based composites [24]. Thus, it can be inferred that the samples prepared under visible light irradiation give rise to a higher amount of isolated gold nanoparticles compared with those prepared under UV irradiation (this interesting phenomenon needs further investigation). In all cases the gold nanoparticles' average size was $\approx$50 nm.

3.2.3. The WO$_3$ and TiO$_2$'s crystallinity related aspects – Raman spectroscopy – Fig. 7

As expected, the only titania crystal phase present in the composite was anatase, as shown by the characteristic bands at 144, 197, 394, 512 and 638 cm^{-1} (the first two bands are not included due to the figure complexity reasons) [31,32]. Neither rutile nor brookite related signals were recorded. The WO$_3$ component of the composites also showed several Raman signals. One of them, as expected, was the band at 810 cm^{-1}, which was relatively weak, broad and it is given by the crystalline WO$_3$. This observation is in agreement with the XRD, where only an extremely small fraction of WO$_3$ was detected (Fig. 7).

Similarly, to the P25 based composites [24] the amorphous species were indicated by the bands centered at $\approx$250–260 cm^{-1} (O–W–O bending modes), 950–960 cm^{-1} (W=O stretching) [8] and 1126 cm^{-1} (four coordinated tungsten species). Additionally, in the case of visible light driven gold deposition the Raman signals were quite distorted due to the intense backscattered light and therefore are not presented here. Despite the low data quality, the Raman spectra of the Aero/WO$_3$(4%), Aero/WO$_3$(4%)–Au–UV,
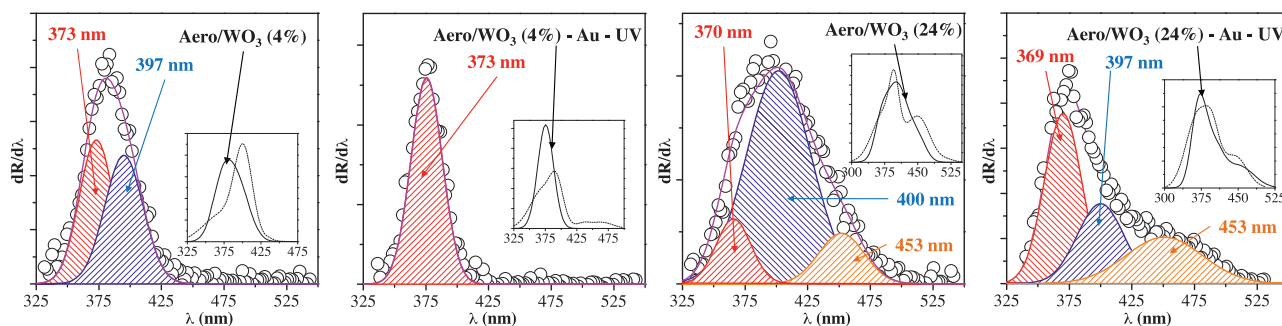

Fig. 6. First order derivative DRS spectra of the selected aerogel based nanomaterials. In the inset figure the dR/dλ curves are superposed of the correspondent composites (P25 based vs. aerogel based).
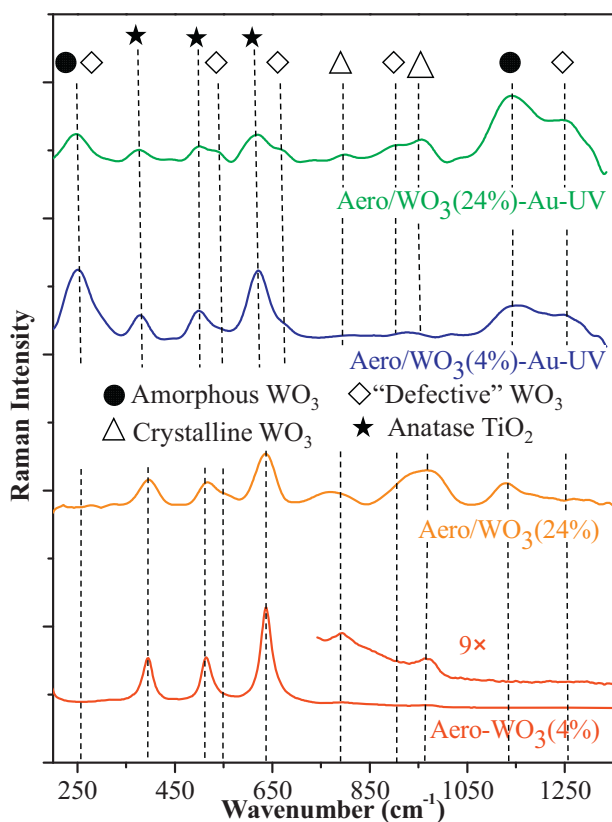
Fig. 7. Crystallinity related aspects' investigation by Raman spectroscopy (In the case of sample Aero/WO$_3$(4%) a 9 factor zoom was also provided).

Aero/WO$_3$(24%) and Aero/WO$_3$(24%)–Au–UV revealed crucial information about the evolution of the tungsten oxide's structure in these materials.

In the sample Aero/WO$_3$(4%) both crystalline and amorphous phases of tungsten oxide were detected (bands at 810 and 950–960 cm^{-1}), while the band at 260 cm^{-1}, which was responsible for the O–W–O bending vibration, was absent. As gold is deposited under UV in the Raman spectra of Aero/WO$_3$(4%)–Au–UV the mentioned band reappears. The same behavior was also observed when the composites contained 24 wt.% WO$_3$. This means that the gold deposition results in a higher "amount" of O–W–O bonds, which according to the literature [33,34] is a sign of a defective crystalline structure.

3.2.4. The surface chemistry of the TiO$_2$/WO$_3$–Au composites – Fig. 8

As shown until now, a few interesting tungsten species and doping was detected by Raman, Diffuse Reflectance Spectroscopy and X-ray diffraction, together with defective and amorphous WO$_3$. It is essential to find out if their presence is significant on the catalysts' surface, because the photocatalytic processes' "action zone" is always the surface of the nanoparticles (Fig. 8).

From the XPS spectra of these materials the following entities were identified (the binding energy values were listed on Table 2 for those species that will be further studied in-detail, the other binding energy values are listed in the first part of the present work):

- W^{6+}: Signal emerged from the crystalline/amorphous WO$_3$ [35,36].
- W^{4+}: Mostly it can be attributed to the amorphous WO$_3$ [35,36].

- W$_{def}$: Defective WO$_x$ entities, where W could possess mixed oxidation states [35,36].
- Ti^{4+}: The main oxidation state in titania containing samples (crystalline) [37,38].
- Ti^{3+}: Reduced form, sometimes indicates the presence of oxygen vacancies [39].
- TiO$_x$–W: Suggests doping or dangling WO$_x$ entities on the surface [40].
- O$_{def}$: Oxygen defects, appearing as low energy oxygen types and they are related to the presence of Ti^{3+} [26].
- Other oxygen species: oxygen from the surface OH, oxide O (both from TiO$_2$ and WO$_3$) [26]
- Au^0: The oxidation state of gold found on the studied nanocomposites. Variations in both, Au4f core level and VB (valance band) spectra was observed and may be associated with the Au atoms distribution on the composite surface [41,42]. This latter observation was reinforced by the DRS spectra.

While no real reference can be appointed for the effect of the tungsten (VI) oxide content (due to the fact that the WO$_3$-free aerogel contains a significant amount of rutile and the crystallite sizes are also quite different), the impact of the additional quantity of WO$_3$ was clearly observable. As expected, the ratio of the W^{6+} increased significantly from 78.9% to 89.2% in the W4f XP spectra of the Aero/WO$_3$ (24%) sample. Concomitantly, in these materials the ratio of the W^{4+} entities remained constant at ≈10.9%. It was observed that the W defects totally disappeared (in the Aero/WO$_3$(4%) composite – 10.0%) from the XPS spectra after raising the WO$_3$ ratio to 24 wt.%. The variations in the ratio of the different W species showed an interesting correlation with the different Ti types. As the fraction of W^{6+} increases so the ratio of the Ti^{3+} decreases from 5.9% to 1.8%, while the TiO$_x$–W species presence was nullified from 11.8%. The changes observed in the surface chemistry clearly indicate that at higher WO$_3$ content the amount of crystalline WO$_3$ increases. Furthermore, no defective tungsten species were detected in sample Aero/WO$_3$(24%), meaning that the crystalline WO$_3$ particles present less defects (meaning that defects still could exists, but they are probably located in the bulk material of the particles).

The gold deposition performed under UV light induced major changes on the chemical nature of the catalysts' surfaces (Aero/WO$_3$((4%)–Au–UV, Aero/WO$_3$(24%)–Au–UV). In each case an increase was noticed in the ratio of W^{6+} (≈2–3% increase, Table 2), while the same ratio value decrease was observed for the W^{4+}. Similar trend was recorded from 5.9% to 4.1% for Aero/WO$_3$(4%)–Au–UV. The situation reversed when the gold was deposited on the composite with the higher WO$_3$ content (1.8–3.1%, sample Aero/WO$_3$(4%)–Au–UV). Additionally, a slight increase was also noticed in the ratio of W$_{def}$ from 10.0% to 12.0%. As for the other studied entities, like TiO$_x$–W, the gold deposition did not influence significantly their presence. The gold nanoparticles deposited under UV light acted as a "propagator" of the crystallization/coordination sphere completion process, because the "unsaturated" W^{4+}s were "patched up to W^{6+}" and the defects present in the crystal lattice of titania/WO$_3$ were "fixed" (which was indicated by the decrease of Ti^{3+}). During this repair process the quantity of defective WO$_3$ increased, indicating an uncompleted structural transition. A single contradictory case was noticed, namely the increase of the Ti^{3+} in the Aero/WO$_3$(24%)–Au–UV composite, where an appropriate explanation of the phenomenon is still necessary.

The situation was slightly different when sample Aero/WO$_3$(4%)–Au–VIS was examined more carefully. The same specie evolution trends were recorded as for sample Aero/WO$_3$(4%)–Au–UV, the main difference consisted in the increase of the W$_{def}$ ratio from 10.0% to 17.0%. As for the composite
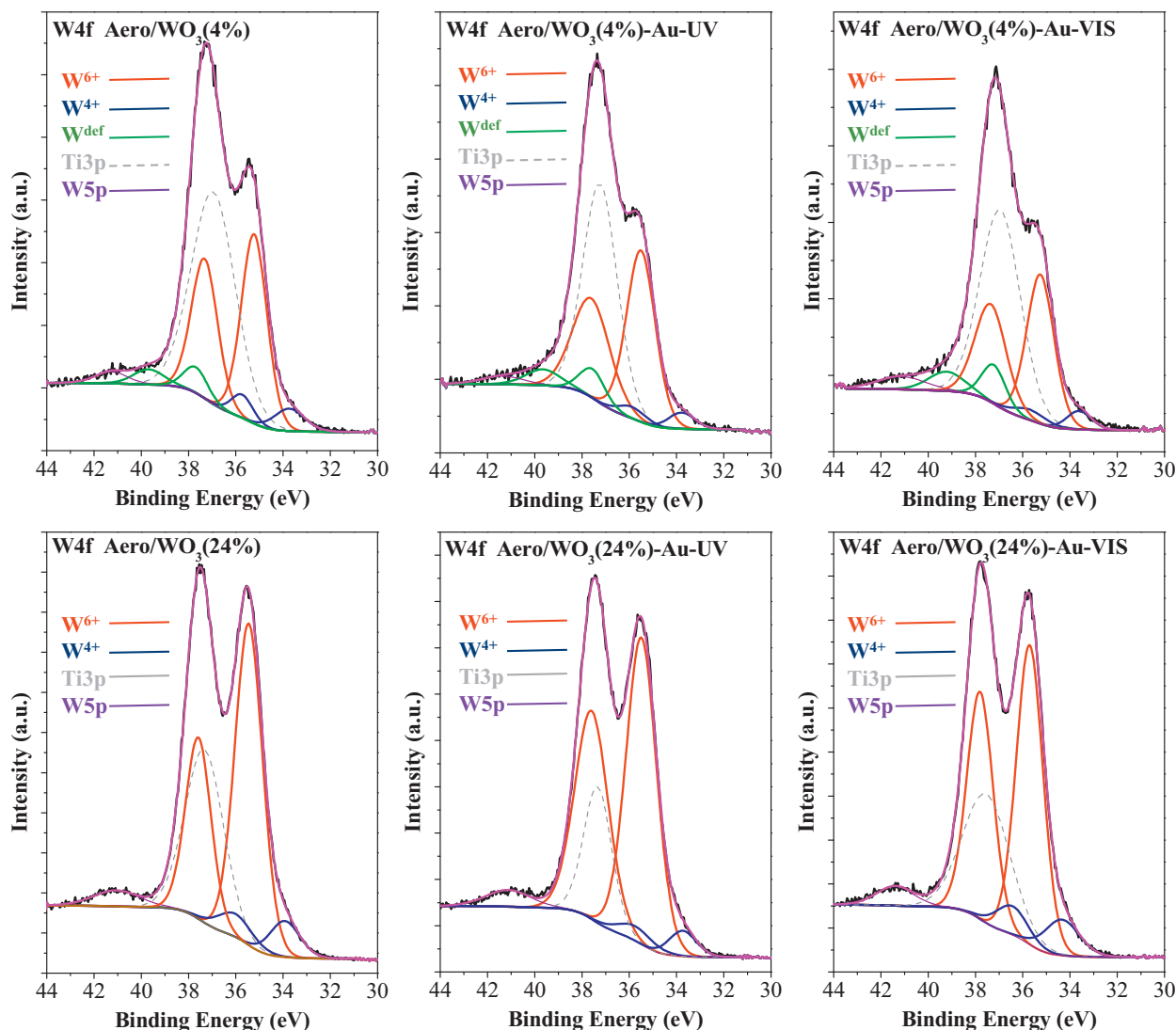
Fig. 8. W4f XP spectra of all the investigated composites.

Aero/WO₃(24%)–Au–VIS, a destabilizing of the surface occurred, because of the significant increase both in Ti³⁺ (from 1.8% to 4.8%) and W⁴⁺ (from 10.8% to 13.4%), while the more stable W⁶⁺ decreased (89.2–86.6%). It seems that the visible light deposition of gold favors the formation of instability points, which occasionally could act as recombination centers.

Furthermore, it should be noted here that in all the investigated materials the oxygen defects are omnipresent (around 528 eV,

approximated concentration of 1%), being usually a crucial factor in defining the achieved activity, which is not the present case.

3.2.5. In-depth structural information obtained via XAFS

Being an element sensitive technique applicable to any state of matter, X-ray absorption spectroscopy (XAS) is probing the bulk of the present composites that have a relatively low surface/volume ratio. The XAS spectra of TiO_2–WO_3 samples containing 24 wt.% of

Table 2
Representative species and their ratio in the studied nanocomposites.

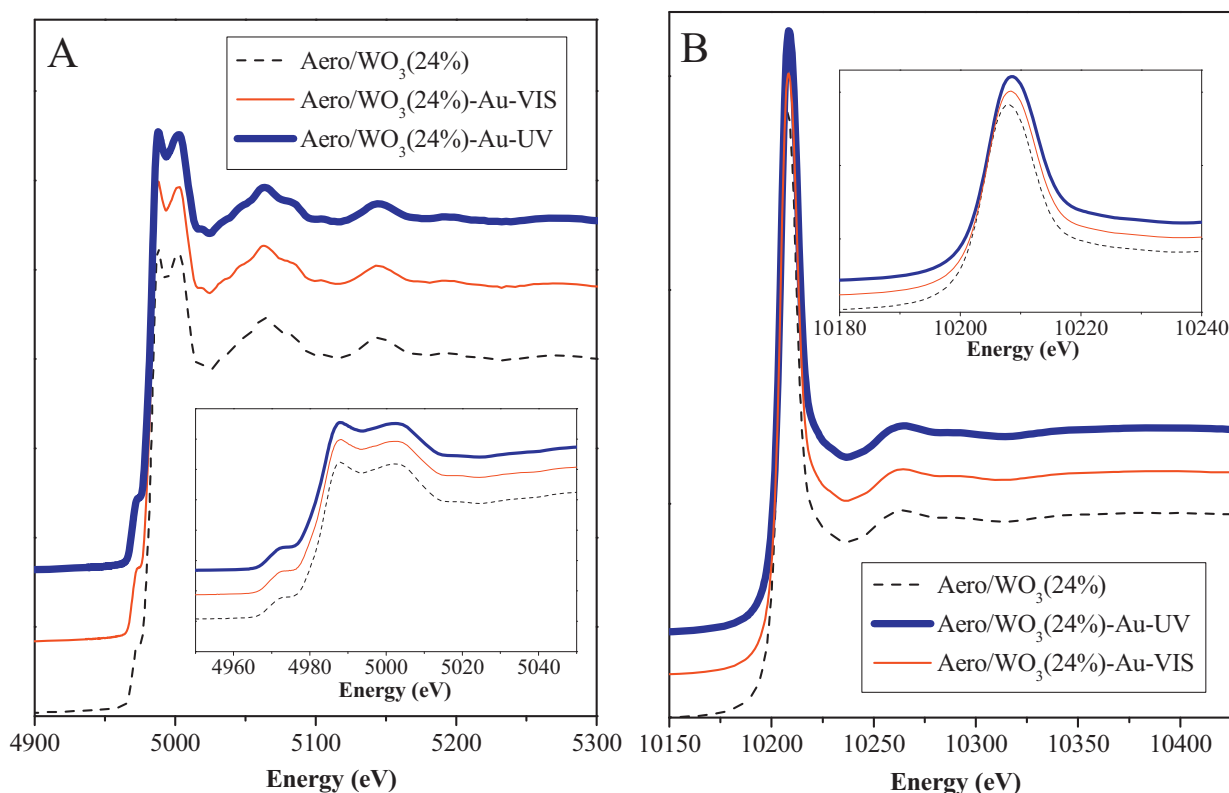| Sample name	Normalized phenol degradation rates (mM/h × m⁻²)	Representative species detected by XPS				
		Total Ti = 100%		Total W = 100%		
		457.2, 461.2 eV Ti³⁺ (%)	459.3, 465.4 eV TiOₓ–W (%)	35.5, 37.6 eV W⁶⁺ (%)	33.7, 35.8 eV W⁴⁺ (%)	37.5, 39.7 eV W_def (%)
Aero/WO₃(4%)	5.73	5.9	11.8	78.9	11.0	10.0
Aero/WO₃(4%)–Au–VIS	–	2.8	12.2	74.6	8.4	17.0
Aero/WO₃(4%)–Au–UV	5.34	4.1	11.7	80.8	7.1	12.1
P25	4.94	–	–	–	–	–
Aero/WO₃(24%)	0.37	1.8	–	89.2	10.8	–
Aero/WO₃(24%)–Au–VIS	–	4.8	–	86.6	13.4	–
Aero/WO₃(24%)–Au–UV	0.38	3.1	-	93.0	7.0	–

Fig. 9. (A) Ti K-edge XAS spectra for Aero/WO$_3$(24%), Aero/WO$_3$(24%)–Au–VIS and Aero/WO$_3$(24%)–Au–UV. (B) W L3-edge XAS spectra for Aero/WO$_3$(24%), Aero/WO$_3$(24%)–Au–VIS and Aero/WO$_3$(24%)–Au–UV. The insets are showing the details of the XANES regions.

WO$_3$ were obtained to investigate the local environment of the Ti and W atoms and effects of gold deposition methods on the coordination state and geometry of Ti and W.

3.2.5.1. Ti K edge.

3.2.5.1.1. XANES region. The normalized X-ray absorption coefficients at the Ti K edge are shown in Fig. 9a. The inset zooms on the XANES region, which spans ~50 eV above the 1s ionization threshold. The 3 spectra are very similar, indicating that the local bonding environment around the Ti center does not vary significantly upon gold deposition. The spectral features differ from the ones observed for the anatase phase, especially with a broad pre-edge peak 1s → 3d centered around 4973 eV. The post-edge region is attributed s to unresolved 3s → np dipole-allowed transitions. The overall spectral shape is nevertheless reminiscent of the one observed for other sol–gel titanium oxides [43,44].

3.2.5.1.2. EXAFS region. Fig. 10a–c shows the Fourier transformed EXAFS oscillations after the Ti K-edge for the Aero/WO$_3$(24%) sample (black) and the samples containing deposited gold under VIS and UV light, Aero/WO$_3$(24%)–Au–VIS (red) and Aero/WO$_3$(24%)–Au–UV (blue). Their respective fitted curves are plotted as grey, orange and cyan lines. The best fit parameters for the EXAFS data are given in Table 3. The coordination number, N, and the nearest Ti–O/Ti–Me (Me = Ti or W) interatomic distance *R* were evaluated via the best fit of $k3x$ (k), calculated by inverse Fourier transform of the moduli, to the theoretical one, using a non-linear least squares method. It can be seen from Table 3 and Fig. 10a–c that the local structure of the three samples are very similar. The structural parameters of first shell Ti–O differ significantly from the standard bulk crystallographic data for octahedral anatase structure. In anatase, there are two different nearest-neighbor Ti–O distances: four Ti–O bonds

at 1.94 Å and two at 1.97 Å. The Aero/WO$_3$(24%) sample has an average Ti–O distance at 1.96 Å and a coordination number of 3.99. The Aero/WO$_3$(24%)–Au–VIS and Aero/WO$_3$(24%)–Au–UV samples have an average distance of 1.95 Å and a coordination number of 3.61 and 3.5, respectively. All of the three samples show to have the Ti–Me distances at ~3.1 and ~3.7 Å, which is characteristic of the Ti–Ti distances in anatase.

3.2.5.2. W L3 edge.

3.2.5.2.1. XANES region. The normalized X-ray absorption coefficients at the W L3 edge are shown in Fig. 9b for Aero/WO$_3$(24%) (black), Aero/WO$_3$(24%)–Au–VIS (red) and Aero/WO$_3$(24%)–Au–UV (blue). The inset zooms on the white line, which is assigned to the 2p → 5d transition. The 3 spectra are clearly similar, indicating that the local bonding environment around the W center does not vary significantly upon gold deposition. The sharp white line is an unambiguous signature of a 4 fold coordination for the W^{6+} ions [45].

3.2.5.2.2. EXAFS region. Fig. 10d–f shows the Fourier transformed EXAFS oscillations after the W L3-edge for the Aero/WO$_3$(24%) sample (black) and the samples containing deposited gold under VIS and UV light, Aero/WO$_3$(24%)–Au–VIS (red) and Aero/WO$_3$(24%)–Au–UV (blue). Their respective fitted curves are plotted as grey, orange and cyan lines. The best fit parameters for the EXAFS data are given in Table 3. The coordination number, N, and the nearest W–O/Ti–Me (Me=Ti or W) interatomic distance *R* were evaluated via the best fit of $k3x$ (k), calculated by inverse Fourier transform of the moduli, to the theoretical one, using a non-linear least squares method. It can be seen from Table 3 and Fig. 10d–f that the local structure in the WO$_3$ amorphous phase is very similar for the 3 samples, meaning that the differently coordinated W is situated only
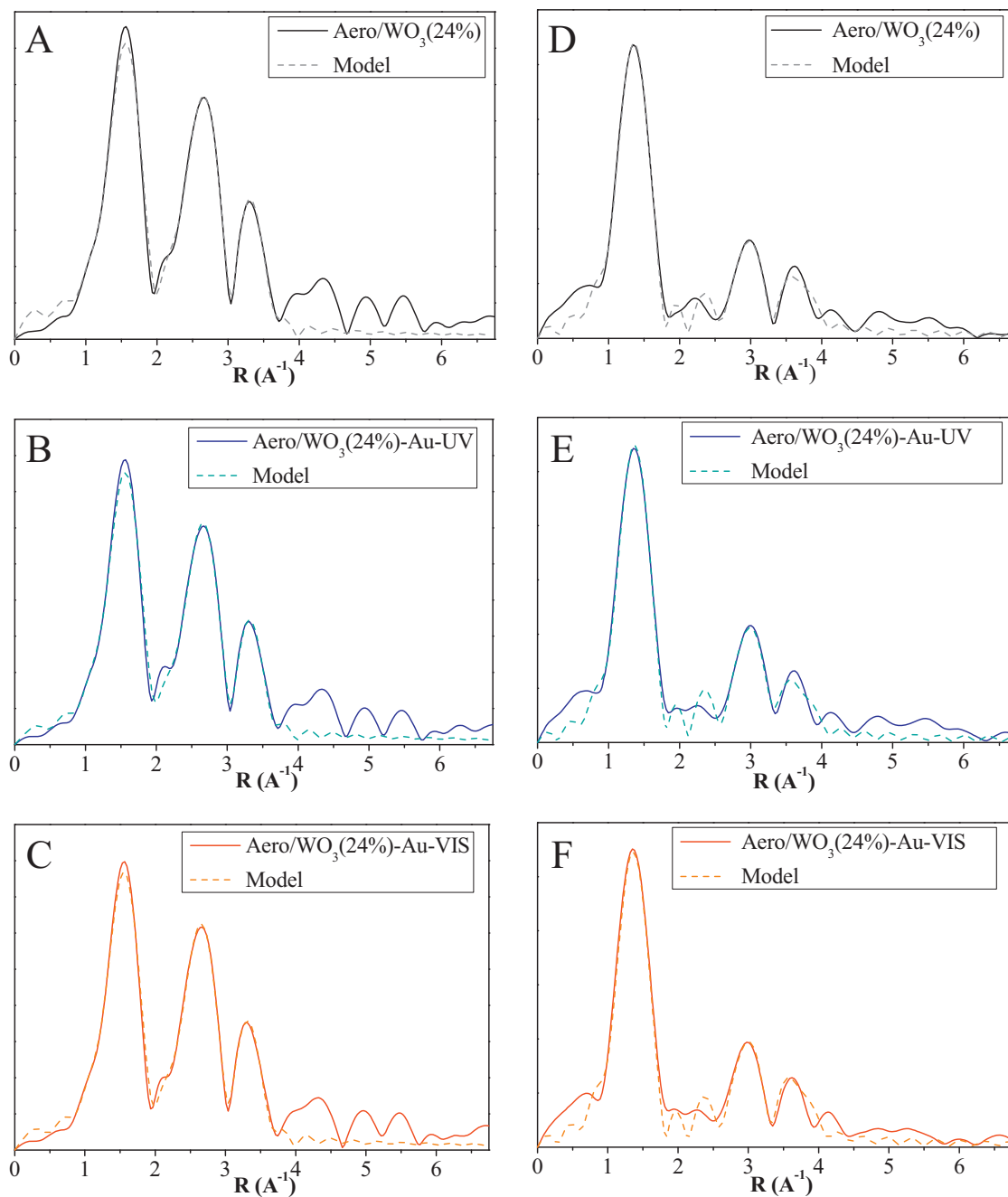
Fig. 10. Fourier transformed EXAFS oscillations and their fits at: (i) the Ti K-edge for the Aero/WO₃(24%) (A), Aero/WO₃(24%)–Au–UV (B) Aero/WO₃(24%)–Au–VIS (C); (ii) the W L3-edge for the Aero/WO₃(24%) (D), Aero/WO₃(24%)–Au–UV (E) and Aero/WO₃(24%)–Au–VIS (F).

Table 3
Coordination numbers (N), bond lengths (R) and Debye–Waller factors (2) for the 3 samples as extracted from the EXAFS spectra at the Ti K edge and W L_3-edge.

Sample	Pair	N	R (Å)	σ^2	E0	R–f. (%)	Pair	N	R (Å)	σ^2	E0	R–f. (%)
Aero/WO₃(24%)	Ti–O	3.99	1.96	0.007	0.83	4.55	W–O	2.18	1.79	0.005	1.50	7.5
	Ti–Ti	3.75	3.10	0.008			W–Ti	1.39	3.22	0.006		
	Ti–Ti	1.53	3.73	0.003			W–W/Ti	1.43	3.75	0.005		
Aero/WO₃(24%)–Au–VIS	Ti–O	3.50	1.95	0.007	3.67	5.06	W–O	2.39	1.80	0.006	0.42	8.9
	Ti–Ti	3.23	3.08	0.008			W–Ti	1.64	3.24	0.006		
	Ti–Ti	1.40	3.73	0.003			W–W/Ti	1.43	3.77	0.005		
Aero/WO₃(24%)–Au–UV	Ti–O	3.61	1.95	0.007	2.83	2.99	W–O	2.24	1.80	0.005	0.38	7.6
	Ti–Ti	3.23	3.08	0.008			W–Ti	1.63	3.22	0.005		
	Ti–Ti	1.48	3.72	0.003			W–W/Ti	1.48	3.76	0.006		

Table 4
Linking structural properties to the intermediates of the phenol UV-photodegradation.

Intermediate	Influence scores																													
	a	b	c	a	b	c	a	b	c	a	b	c	a	b	c	a	b	c	a	b	c	a	b	c	a	b	c	a	b	c
HC	+	0	0	+	−	+	+	+	−	+	0	−	+	0	+	−	−	−	−	0	0	+	+	−	0	−	+	−	+	0
PY	−	0	−	−	−	−	+	+	−	0	−	0	−	0	−	+	−	+	−	0	0	−	+	+	0	−	−	+	+	0
RES	−	0	0	−	+	+	−	−	+	0	−	+	−	0	−	+	+	+	+	0	0	−	−	+	0	+	−	+	−	0
124THB	0	0	0	0	+	0	0	−	0	0	0	0	0	0	0	0	+	0	0	0	0	0	−	0	0	+	0	0	−	0
Cumulative influence	−1			0			0			0			−2			+2			+1			0			−1			+1		
Parameter	Crystallinity XRD			Doping DRS			Amorphous Raman			Defective Raman			BET area			Ti³⁺ XPS			TiOₓ–W XPS			W⁶⁺ XPS			W⁴⁺ XPS			W_def XPS		
Information zone	Bulk (total influence:1)												Surface (total influence: 7)																	

a, the addition of WO$_3$ in 24 wt.%; b, the UV deposition of gold on 4 wt.% WO$_3$ containing composites; c, the UV deposition of gold on 24 wt.% WO$_3$ containing composites.

on the surface of the crystallites as was well pointed out by XPS.

3.3. Linking the obtain data to structural information provided by the other conventional characterization methods

This section is entirely based on the data presented in Table 4 and details the delicate relationship between the observed degradation by-products and structural features. The quantification of the influence was performed as follows: if a parameter increase raised the IEI value, than the gained value is +, while in the case of opposite impact (positive parameter increase, negative influence on the IEI value), the given value is −. Additionally, if no "reaction" was noticed in the IEI value during a structural parameter change or vice versa, the influence was considered 0[2].

Some of these peculiarities are linked among them (discussed previously), but their localization is quite different (i.e. defective crystallization in the bulk vs. W$_{def}$ detected on the surface). The following ten "structural" groups can be found:

1. *Bulk crystallinity*. Influence grade was −1: As the degree of the sample crystallization increases, the intermediate formation is inhibited.
2. *W-doping*: Influence grade was 0: Despite to this value, in the case of PY is a quite clear "−" effect
3. *Amorphous WO$_3$ entities*: Influence grade was 0: No clear relations were established with the degradation intermediates
4. *Defective bulk WO$_3$*: Influence grade was 0: One of the most unclear parameter. Further investigations are needed.
5. *Surface area*: Influence grade was −2: Strangely it means that higher BET values mean lower IEI values. This results gets logical if we take in account the fact that phenol can be complexated at the surface of WO$_3$, meaning a higher surface coverage, lower possibility to release intermediates.
6. *Ti³⁺*: Influence grade was +2: With the increase of reduced titania sites, the possibility to obtain higher IEI values is high. Also can be related to the activity of titanias as we showed recently [26].
7. *TiO$_x$–W*: Influence grade was +1: This interesting species on the surface favored the IEI value increase trough the possible facilitation of the phenol complexation.
8. *W⁶⁺*: Influence grade was 0: As expected, the species which represents partially all other W species classes is independent from the IEI value variations.
9. *W⁴⁺*: Influence grade was −1: The presence of tungsten in this oxidation state induces an instability factor to the catalysts, which means, usually a lower activity and, consequently lower IEI.
10. *W$_{def}$*: Influence grade was +1: Defective tungsten oxide on the surface of the nanoparticles proved to have a positive impact on the IEI variation. Also suggests and affirms the possibility of the complexation process.

The summarized influence factor was also evaluated for each category of species. Namely, in the case of bulk entities the summarized influence score (the numbers were added in modulus) was 1, while in the case of surface species was 7. It is clear that the surface is at least one order of magnitude more important.

4. Conclusions

In the present work it was shown that the build-up (synthesis pathway) of a catalyst cannot be neglected, due to the strong relationship between the structural features and degradation intermediates, which are extremely important if water purification is one of the target applications of these materials. It was shown, that the composite's composition, the gold deposition mode (under UV or visible) were found to be crucial, trough the different structural peculiarities, such as different Ti, W species present in the bulk and on the surface of the nanostructures or the crystallinity of the WO$_3$. The "geometrical element" containing the investigated influence factors was clearly the surface. Crucial influence was attributed to the starting materials, because major differences were observed in the activity/intermediates and structures if these composites were obtained through impregnation (from Aeroxide P25 [24]) or sol/gel (trough aerogel). Furthermore, these results should encourage other researchers to do similar investigations on their materials to get vital information about their functionality and future safety.

---

[2] Please take into account the fact that the magnitude of each parameters' impact (which is nearly impossible to determine individually) was not considered in the quantification process.

Appendix A. Supplementary data

Supplementary data associated with this article can be found, in the online version, at http://dx.doi.org/10.1016/j.apcatb.2013.12.034.

References

[1] A. Fujishima, T.N. Rao, D.A. Tryk, J. Photochem. Photobiol. C: Photochem. Rev. 1 (2000) 1–21.
[2] A. Fujishima, K. Honda, S. Kikuchi, J. Soc. Chem. Ind. Jpn. 72 (1969) 108–113.
[3] C.-F. Lin, C.-H. Wu, Z.-N. Onn, J. Hazard. Mater. 154 (2008) 1033–1039.
[4] C.M. Carney, S. Yoo, S.A. Akbar, Sens. Actuat. B: Chem. 108 (2005) 29–33.
[5] Ö. Kesmez, H. Erdem Çamurlu, E. Burunkaya, E. Arpaç, Solar Energy Mater. Solar Cells 93 (2009) 1833–1839.
[6] T. Ohno, S. Tagawa, H. Itoh, H. Suzuki, T. Matsuda, Mater. Chem. Phys. 113 (2009) 119–123.
[7] É. Karácsonyi, L. Baia, A. Dombi, V. Danciu, K. Mogyorósi, L.C. Pop, G. Kovács, V. Coşoveanu, A. Vulpoi, S. Simon, Zs. Pap, Catal. Today 208 (2013) 19–27.
[8] K.K. Akurati, A. Vital, J.-P. Dellemann, K. Michalow, T. Graule, D. Ferri, A. Baiker, Appl. Catal., B 79 (2008) 53–62.
[9] Y.-C. Nah, A. Ghicov, D. Kim, S. Berger, P. Schmuki, J. Am. Chem. Soc. 130 (2008) 16154–16155.
[10] J.H. Park, O.O. Park, S. Kim, Appl. Phys. Lett. 89 (2006) 163106–163106-3.
[11] C.W. Lai, S. Sreekantan, Int. J. Hydrogen Energy 38 (2013) 2156–2166.
[12] P.V. Kamat, Abstr. Pap. Am. Chem. Soc. (2007) 233.
[13] Zs. Pap, A. Radu, I.J. Hidi, G. Melinte, L. Diamandescu, T. Popescu, L. Baia, V. Danciu, M. Baia, Chin. J. Catal. 34 (2013) 734–740.
[14] M. Popa, D. Macovei, E. Indrea, I. Mercioniu, I.C. Popescu, V. Danciu, Microporous Mesoporous Mater. 132 (2010) 80–86.
[15] D. D'Elia, C. Beauger, J.-F. Hochepied, A. Rigacci, M.-H. Berger, N. Keller, V. Keller-Spitzer, Y. Suzuki, J.-C. Valmalette, M. Benabdesselam, P. Achard, Int. J. Hydrogen Energy 36 (2011) 14360–14373.
[16] M. Popa, E. Indrea, P. Pascuţa, V. Coşoveanu, I.C. Popescu, V. Danciu, Rev. Roum. Chim. 55 (2010) 369–375.
[17] Zs. Pap, V. Danciu, Z. Cegléd, Á. Kukovecz, A. Oszkó, A. Dombi, K. Mogyorósi, Appl. Catal., B 101 (2011) 461–470.
[18] G. Veréb, Z. Ambrus, Zs. Pap, Á. Kmetykó, A. Dombi, V. Danciu, A. Cheesman, K. Mogyorósi, Appl. Catal., A 417–418 (2012) 26–36.
[19] H. Zhang, J.F. Banfield, J. Phys. Chem. B 104 (2000) 3481–3487.
[20] R. Jenkins, R.L. Snyder, Introduction to X-ray Powder Diffractometry, John Wiley & Sons, New York, 1996.
[21] D. Flak, A. Braun, B.S. Mun, J.B. Park, M. Parlinska-Wojtan, T. Graule, M. Rekas, Phys. Chem. Chem. Phys. 15 (2013) 1417–1430.
[22] S. Carlson, M. Clausen, L. Gridneva, B. Sommarin, C. Svensson, J. Synchrotron Radiat. 13 (2006) 359–364.
[23] K.V. Klementev, J. Phys. D Appl. Phys. 34 (2001) 209–217.
[24] G. Kovács, L. Baia, A. Vulpoi, T. Radu, É. Karácsonyi, A. Dombi, K. Hernádi, V. Danciu, S. Simon, Zs. Pap, Appl. Catal., B 147 (2014) 508–517.
[25] Y. Wen, B.T. Liu, W. Zeng, Y.H. Wang, Nanoscale 5 (2013) 9739–9746.
[26] Zs. Pap, É. Karácsonyi, Z. Cegléd, A. Dombi, V. Danciu, I.C. Popescu, L. Baia, A. Oszkó, K. Mogyorósi, Appl. Catal., B 111–112 (2012) 595–604.
[27] S. Cao, K. Yeung, P. Yue, Appl. Catal., B 68 (2006) 99–108.
[28] J.Z. Zhang, Optical Properties and Spectroscopy of Nanomaterials, World Scientific Publishing Co. Pte. Ltd., Singapore, 2009.
[29] M. Baia, L. Baia, S. Astilean, Chem. Phys. Lett. 404 (2005) 3–8.
[30] F. Toderas, M. Baia, L. Baia, S. Astilean, Nanotechnology 18 (2007) 255702.
[31] D. Georgescu, L. Baia, O. Ersen, M. Baia, S. Simon, J. Raman Spectrosc. 43 (2012) 876–883.
[32] L. Baia, A. Peter, V. Cosoveanu, E. Indrea, M. Baia, J. Popp, V. Danciu, Thin Solid Films 511–512 (2006) 512–516.
[33] A. Baserga, V. Russo, F. Di Fonzo, A. Bailini, D. Cattaneo, C.S. Casari, A. Li Bassi, C.E. Bottani, Thin Solid Films 515 (2007) 6465–6469.
[34] S. Chan, I. Wachs, L. Murrell, N. Dispenziere, J. Catal. 92 (1985) 1–10.
[35] D.M. Chen, G. Xu, L. Miao, L.H. Chen, S. Nakao, P. Jin, J. Appl. Phys. (2010) 107.
[36] G. Leftheriotis, S. Papaefthimiou, P. Yianoulis, A. Siokou, Thin Solid Films 384 (2001) 298–306.
[37] A.B. Boffa, H.C. Galloway, P.W. Jacobs, J.J. Benitez, J.D. Batteas, M. Salmeron, A.T. Bell, G.A. Somorjai, Surf. Sci. 326 (1995) 80–92.
[38] M.S. Chen, W.T. Wallace, D. Kumar, Z. Yan, K.K. Gath, Y. Cai, Y. Kuroda, D.W. Goodman, Surf. Sci. 581 (2005) L115–L121.
[39] J.T. Mayer, U. Diebold, T.E. Madey, E. Garfunkel, J. Electron. Spectrosc. 73 (1995) 1–11.
[40] D. Kumar, M.S. Chen, D.W. Goodman, Thin Solid Films 515 (2006) 1475–1479.
[41] Z. Paszti, G. Peto, Z.E. Horvath, A. Karacs, L. Guczi, Solid State Commun. 107 (1998) 329–333.
[42] T. Radu, D. Benea, R. Ciceo-Lucacel, O. Ponta, S. Simon, J. Appl. Phys. 111 (2012), art. no. 034701.
[43] I. Manzini, G. Antonioli, D. Bersani, P.P. Lottici, G. Gnappi, A. Montenero, J. Non-Cryst. Solids 193 (1995) 519–523.
[44] V. Luca, S. Djajanti, R.F. Howe, J. Phys. Chem. B 102 (1998) 10650–10657.
[45] S. Yamazoe, Y. Hitomi, T. Shishido, T. Tanaka, J. Phys. Chem. C 112 (2008) 6869–6879.